Pressure conditions for shear and tensile failure around a circular magma chamber; insight from elasto-plastic modelling

MURIEL GERBAULT

Université de Nice Sophia-Antipolis, Institut de Recherche pour le Développement (UR 082), Observatoire de la Côte d'Azur, Géoazur, 250 av Einstein 06560 Valbonne, France (e-mail: gerbault@geoazur.unice.fr)

Abstract: Overpressure within a circular magmatic chamber embedded in an elastic half space is a widely used model in volcanology. However, this overpressure is generally assumed to be bounded by the bedrock tensile strength since gravity is neglected. Critical overpressure for wall failure is thus greater. It is shown analytically and numerically that wall failure occurs in shear rather than in tension, because the Mohr–Coulomb yield stress is less than the tensile yield stress. Numerical modelling of progressively increasing overpressure shows that bedrock failure develops in three stages: (1) tensile failure at the ground surface; (2) shear failure at the chamber wall; and (3) fault connection from the chamber wall to the ground surface. Predictions of surface deformation and stress with the theory of elasticity break down at stage 3. For wall tensile failure to occur at small overpressure, a state of lithostatic pore-fluid pressure is required in the bedrock which cancels the effect of gravity. Modelled eccentric shear band geometries are consistent with theoretical solutions from engineering plasticity and compare well with shear structures bordering exhumed intrusions. This study shows that the measured ground surface deformation may be misinterpreted when neither plasticity nor pore-fluid pressure is accounted for.

Supplementary material: The numerical benchmark data are available at: http://www.geolsoc.org.uk/SUP18517.

An unsolved question in volcanology is that of the conditions for and progression of country rock failure around near-surface pressurized magma bodies. Anderson (1936) was the first to apply mathematical solutions derived from the theory of elasticity to explain the formation of cone-sheets and ring-dykes around circular igneous intrusions: 'In explaining central intrusions it is necessary to involve both types of rupture, the tensile type to produce cone-sheets, and the shearing-type to account for the production of ring-dykes, giving rise to nearly vertical ring-fractures'. Despite several decades of analytical and numerical models of deformation around magmatic chambers (e.g. reviews by Acocella 2007; Marti *et al.* 2008; Geyer & Marti 2009) and a considerably longer history of field studies examining exposed structures (e.g. Gudmundsson 2006), many questions remain. The crude state of our knowledge with respect to magma chamber deformation is also revealed with the application of elastic models to geodetic monitoring of active volcanoes (e.g. Mogi 1958; Masterlark 2007; Segall 2009). As the non-unique fit between measured and modelled deformation spans a wide range of parameters (chamber geometry, country rock rheology, pore pressure and magmatic overpressure, etc.) it is clear that more constraints are desirable. One fundamental approach is to simulate the failure patterns that arise from an idealistic volcanic chamber with a minimum number of parameters; this is the objective of this work.

In this paper it is shown, analytically and numerically, how commonly used solutions of critical overpressure for bedrock failure can be biased when neglecting the role of gravity. Whereas Grosfils (2007) raised this problem of yield stress conditions for tensile failure around a circular magmatic chamber, here it is demonstrated how in fact shear failure should theoretically occur rather than tensile failure. Previous models that use self-consistent elasto-plasticity or visco-elasto-plasticity have not directly addressed the critical pressure condition for bedrock failure. As a matter of fact, the precise state of internal pressure associated with the initiation and propagation of faulting around an idealistic circular magmatic chamber remains poorly constrained.

First, the conditions for failure around a circular pressurized inclusion are developed. The reasoning is then supported with numerical models that incorporate self-consistent elasto-plasticity with a Mohr–Coulomb failure criterion. The progression of plastic yielding is explored, displaying peculiar geometrical patterns that are produced with increasing internal overpressure, and their similarity to solutions from engineering plasticity are demonstrated.

From: Healy, D., Butler, R. W. H., Shipton, Z. K. & Sibson, R. H. (eds) 2012. *Faulting, Fracturing and Igneous Intrusion in the Earth's Crust*. Geological Society, London, Special Publications, **367**, 111–130. http://dx.doi.org/10.1144/SP367.8

The role of pore-fluid pressure is also illustrated, as it nullifies the gravity component in the shear failure yield criterion and allows for tensile failure to occur instead.

In discussing conditions for shear failure in the real world, a few examples of shearing structures exposed at the borders of magmatic bodies are displayed. The main point of this paper is to show that it is necessary to consider a state of near-lithostatic fluid overpressure in the bedrock in order to explain field observations of tensile failure, predicted to occur for less than or an average of 10 MPa of internal overpressure around an ideal spherical magmatic chamber.

Analytical pressure solutions for tensile and shear failure

Classical solution for tensile failure

Simple solutions of surface displacement over a spherical source, with depth much greater than radius, were approximated by Mogi (1958) using a dilational point source. This solution remains widely used for fitting geodetic measurements above active volcanoes (Bonafede *et al.* 1986; Masterlark & Lu 2004; Pritchard & Simons 2004; Trasatti *et al.* 2005; Ellis *et al.* 2007; Masterlark 2007; Bonafede & Ferrari 2009; Foroozan *et al.* 2010). Crustal deformation in the idealistic elastic crust is assumed to be the result of a pressure change ΔP in the source with respect to 'hydrostatic' pressure. Assuming Poisson's ratio ν is equal to 0.25 and G is the shear modulus, calculated horizontal and vertical displacements at the surface are:

$$u_x = \frac{3\Delta P}{4G}\frac{R^3 x}{(x^2+H^2)^{3/2}}, \quad u_y = \frac{3\Delta P}{4G}\frac{R^3 H}{(x^2+H^2)^{3/2}} \tag{1}$$

where R and H are the radius and the depth of the chamber, respectively (Fig. 1). In plane-strain, the magma chamber becomes an infinitely long cylinder and the analytical solution differs by a factor of about 4 depending on R and H; stress functions for a generic class of problems with complex variables are provided by Verruijt (1998).

The distribution of the stress field produced by a pressurized circular cavity in an elastic half-space was solved by Jeffery (1920) using curvilinear coordinates and plane strain. At the free surface, he showed that the horizontal component of the stress field (σ_{xx}) is:

$$\sigma_{xx} = \frac{-4\Delta P R^2(x^2 - H^2 + R^2)}{(x^2 + H^2 - R^2)^2}. \tag{2}$$

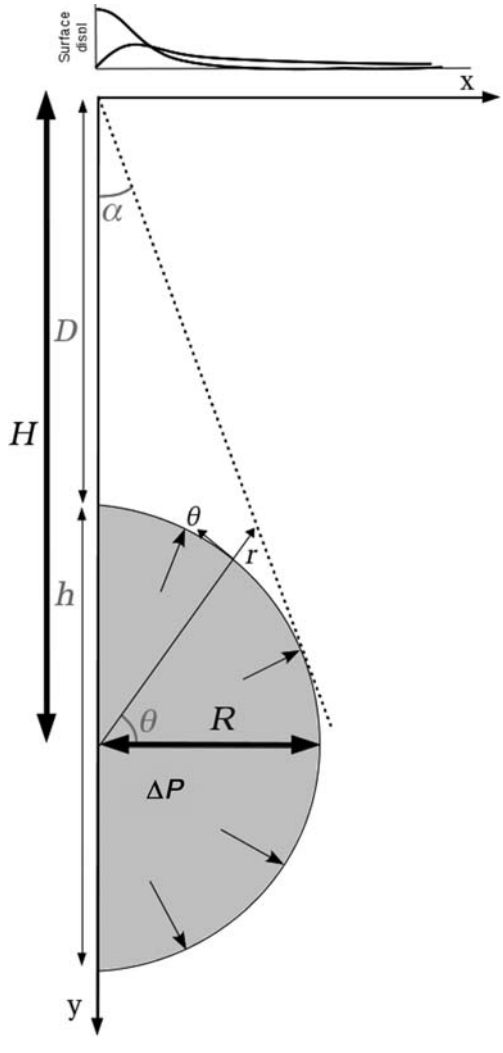

Fig. 1. Parametric definition of the problem. Grey values are those defined by Grosfils (2007).

Its maximum is located above the chamber at X_o, with $\sigma_{xx} = 4\Delta P R^2/(H^2 - R^2)$. At the chamber wall, the hoop stress is expressed according to either the angle α between the vertical axis of symmetry and the line joining the surface origin X_o to a point on the chamber wall (Jeffery 1920) or to the polar angle θ taken from the horizontal at the centre of the chamber to that same point (Grosfils 2007):

$$\sigma_{\theta\theta} = \Delta P(1 + 2\tan^2\alpha). \tag{3}$$

Jeffery (1920) defined the free surface correction factor $C = 1 + 2\tan^2\alpha$, and showed that the hoop stress at the wall is maximum when

$\alpha_m = \arcsin(R/H)$ (Fig. 1). Then, $\sigma_m = -\Delta P(H^2 + R^2)/(H^2 - R^2)$.

Jeffery (1920) also discussed the conditions for failure: 'if H is greater than $R\sqrt{2}$ and less than $R\sqrt{3}$, and internal pressure increased until failure occurs, the crack will begin on the surface according to the greatest tension theory or on the edge of the hole if the greatest stress-difference theory holds'.

The majority of authors, such as Gudmundsson (1988), Tait *et al.* (1989), Gudmundsson *et al.* (1997) and Pinel & Jaupart (2003, 2005), assume that the same tensile failure criterion applies to the Earth's surface and the chamber walls, that is, when the deviatoric stress $(\sigma_1 - \sigma_3)/2$ exceeds the rock's tensile strength T.

- At the surface where the gravity component vanishes, failure occurs when $(\sigma_{xx} - \sigma_{zz})/2 = T$. By combining with Equation (3), the internal overpressure reaches the critical value

$$\Delta P_S = T\left(\frac{H^2 - R^2}{2R^2}\right). \quad (4)$$

- At the chamber wall, the same tensile failure criterion gives $(\sigma_{\theta\theta} - \Delta P)/2 = T$. By combining with Equation (2), the critical internal overpressure is

$$\Delta P_T = T\left(\frac{H^2 - R^2}{H^2}\right). \quad (5)$$

Tensile failure is therefore traditionally predicted to initiate at the previously given location α_m along the chamber wall for magmatic overpressures $\Delta P_T \leq T$, which ranges between *c.* 6 MPa (Gudmundsson *et al.* 2002) and 20 MPa (Pinel & Jaupart 2003).

Grosfils' solution for tensile failure

Grosfils (2007) demonstrated analytically and numerically that a higher critical overpressure was required to initiate wall failure, invoking the necessity to account for the gravity body force. Considering a spherical chamber of equal magma and rock densities, his analytical reasoning is summarized as follows.

(a) The total magma pressure is first defined as the sum of an internal overpressure ΔP and the lithostatic stress, $P_t = \Delta P - \rho g y$.

(b) Grosfils (2007) then proceeded as in previous studies (e.g. Gudmundsson 1988) by assuming that the tangential stress $\sigma_{\theta\theta}$ equals half the normal stress balance across the wall modified by the free surface factor C, so that:

$$\sigma_{\theta\theta} = C\Delta P/2. \quad (6)$$

(c) Grosfils (2007) expressed C as a function of relative depth h taken from the crest of the chamber, itself located at depth $D = H - R$ (Fig. 1):

$$C = 1 + 2\tan^2\alpha = \frac{2h(2R + D) + D^2 - h^2}{(D + h)^2}. \quad (7)$$

C has a parabolic shape >1, and equals 1 when h equals 0 or $2R$.

(d) Differently from previous authors, Grosfils (2007) then argued that tensile failure at the chamber's wall occurs when the tangential stress $\sigma_{\theta\theta}$ exceeds not only the tensile strength of rocks T but also the wall-parallel component of the lithostatic stress P_l, that is

$$\sigma_{\theta\theta} = T + P_l = T + \rho g(D + h). \quad (8)$$

(e) Combining Equations (6) and (8), Grosfils' overpressure for tensile failure $\Delta P = \Delta P_{TG}$ is defined:

$$\Delta P_{TG} = \frac{2T}{C} + 2\rho g\frac{D + h}{C}. \quad (9)$$

In summary, 'the total pressure P_t required for tensile failure approaches the limit of 3 times the lithostatic stress σ_z at great depth ($D \gg R$), whereas it becomes less than σ_z if $R > 0.6D$' (Grosfils 2007). The associated critical overpressure ΔP_{TG} contrasts with the prediction of ΔP_T of failure for only a few MPa above lithostatic pressure (Equation (5), e.g. Tait *et al.* 1989; Gudmundsson *et al.* 1997, 2002; Pinel & Jaupart 2003, 2005; Gudmundsson 2006). Grosfils (2007) discussed in detail how this difference stems from the absence of gravity in the formulation of most analytical models and contrary to the common belief: 'a self-consistent numerical approach that incorporates explicit boundary stresses and body loads becomes a necessary reference against which analytical models should be improved'.

Conditions for shear failure

Now we shall evaluate the internal overpressure (ΔP_{MC}) necessary to produce shear failure in the bedrock surrounding the chamber, and compare it with the above-mentioned overpressure prediction required for tensile failure.

The classical Mohr–Coulomb criterion of failure relates the tangential and normal stresses τ_s and σ_n along any given plane of a medium with internal friction angle φ and cohesion S_o. This

criterion can also be written in terms of the pressure P and the deviatoric shear stress σ_{II}:

$$\tau_s = S_o - \sigma_n \tan\varphi, \quad \tau_s = \sigma_{II}\cos\varphi, \quad \sigma_n = -P + \sigma_{II}\sin\varphi. \tag{10}$$

We first neglect gravity, and assume that the minimum and maximum principal stress components at the chamber wall are of opposite sign so that $P = 0$ and $\sigma_{II} = \Delta P_{MC}$ (ΔP_{MC} is the applied internal overpressure; note that in 3D, $\sigma_{II} = \Delta P_{MC}/2$; Timoshenko & Goodier 1970). When adding gravity, the isotropic lithostatic component appears in the total pressure $P = -\rho g y$ (at negative depth y) which, when inserted into Equation (10), provides:

$$\Delta P_{MC} = S_o \cos\varphi - \rho g y \sin\varphi. \tag{11}$$

In order to account for the free surface (e.g. Gudmundsson 1988; Parfitt *et al.* 1993), the factor C appears in the relationship between the principal stresses at the wall: $\sigma_3 = -C\sigma_1$. The stress invariants P and σ_{II} are then expressed:

$$P = -\rho g y + \Delta P \frac{C-1}{2}, \quad \sigma_{II} = \Delta P \frac{C+1}{2}.$$

Inserting these expressions into the Mohr–Coulomb criterion (Equation (10)) and defining a theoretical tensile strength deduced from the cohesion $T_o = S_o/\tan\varphi$ provides the critical overpressure required for shear failure ΔP_{MCS} :

$$\Delta P_{MCS} = 2\sin\varphi \frac{-\rho g y + T_o}{1 + \sin\varphi + C(1-\sin\varphi)}. \tag{12}$$

At the vertical axis of symmetry where $C = 1$, this expression is equivalent to Equation (11).

Figure 2 displays all three analytical predictions of the internal pressures required for (a) tensile failure at the chamber wall according to classical predictions (Equation (5)), (b) Grosfils' prediction (Equation (9)), and (c) shear failure according to Equation (12). Friction and cohesion are defined as

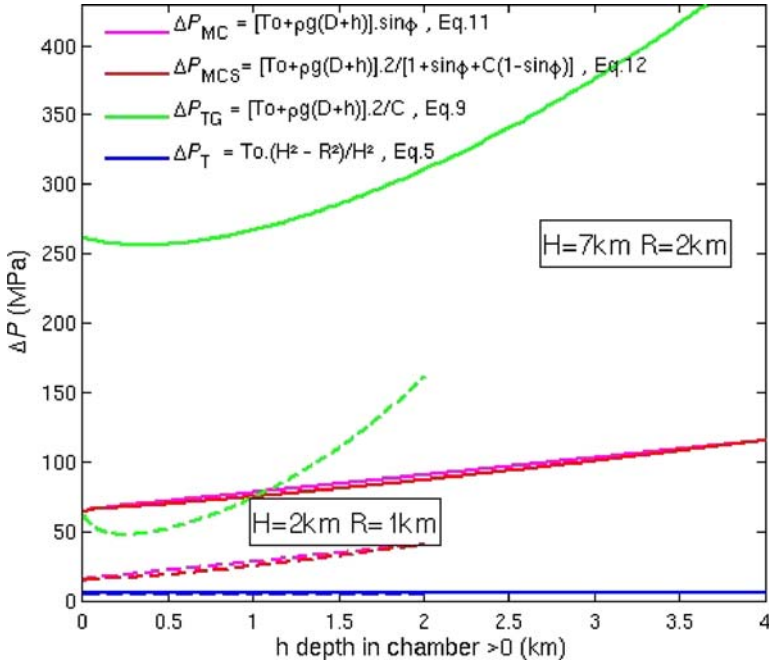

Fig. 2. Pressure difference ΔP required to initiate failure at the chamber wall according to different assumptions: tensile failure accounting for free surface without gravity (ΔP_T, Equation (5)) and with gravity (Grosfils 2007; ΔP_{TG}, Equation (9)) and Mohr–Coulomb shear failure with and without a free surface (ΔP_{MC}, Equation (11); ΔP_{MCS}, Equation (12)). Here both depth and overpressure are set positive. Failure onset is predicted where the critical overpressure is minimal: it initiates at the crest when $H = 7$ km and $R = 2$ km (depth $h = 0$ and angle $\theta = 90^\circ$) and at h *c.* 0.2 km when $H = 2$ km and $R = 1$ km.

$\varphi = 30^\circ$, $S_o = 10$ MPa. Two cases with different depth and radius are displayed, one at depth $H = 7$ km and radius $R = 2$ km ($R/D = 0.4$) and another at depth $H = 2$ km and $R = 1$ km ($R/D = 1$). For both cases, the critical overpressure for shear failure (ΔP_{MC}) is smaller than that for tensile failure when gravity is accounted for. The effect of the free-surface modifies only the internal slope between the crest and the base of the chamber, which indicates that shear failure can initiate over a broad domain extending laterally from the chamber roof.

To summarize, it has been shown that a chamber wall should yield by shear failure (mode II) rather than by tensile failure (mode I).

Predictions from other studies

Many studies have developed analogue and numerical models of failure around a magmatic chamber (e.g. Roche & Druitt 2001; Acocella *et al.* 2004; Acocella 2007; Marti *et al.* 2008) but surprisingly, apart from Grosfils (2007), few directly address the association between the mode of failure, the geometry of the failure domain and the internal overpressure. There are several methodological reasons for this.

First, a majority of studies model only elastic behaviour of the bedrock, and contour the domains that exceed a failure stress threshold that is chosen a priori (e.g. Sartoris *et al.* 1990; Gudmundsson 1988, 2006; Gudmundsson *et al.* 2002; Masterlark 2007). This method has been used since the 1950s (Hafner 1951) but, while it generally yields good results to a first order, it does not account for self-consistent plasticity. This method therefore cannot address when exactly failure initiates with respect to the level of internal magmatic overpressure.

Other models incorporate self-consistent elasto-plasticity, but a dilational deformation is applied instead of an internal overpressure (Chery *et al.* 1991; Kusumoto & Takemura 2003; Gray & Monaghan 2004; Hardy 2008). Only Chery *et al.* (1991) evaluate chamber overpressures of 50–60 MPa around a magmatic chamber 10 km deep embedded in a temperature-dependent elasto-plastic-ductile crust; however, a state of hydrostatic pore-fluid pressure was also assigned in the bedrock, and the precise shape of the associated failure domain was not given (the mesh resolution was poor with a chamber wall composed of 12 elements).

Models that define a magmatic chamber with sharp edges produce failure much 'more easily' than when an ideal circular body is used. For example, Burov & Guillou-Frottier (1999) and Guillou-Frottier *et al.* (2000) modelled a cycle of inflation and collapse with only 10 MPa overpressure, applied in a middle-crust rectangular chamber, with visco-elasto-plastic rheology. In these models, shear band structures develop between the corners of the chamber and the surface.

Finally, Trasatti *et al.* (2005) tested a number of parameters to model surface uplift at Campi Flegrei volcano. Whereas Mogi-type elastic models without gravity reproduced the measured uplift for an internal overpressure of at least 80 MPa (the lithostatic pressure at the chamber's crest *D c.* 3200 m, recognized as unrealistic), elasto-plastic models including gravity and a Von Mises failure threshold set to 15 MPa reproduced the uplift for an internal overpressure of only 45–50 MPa. This study illustrates how greater surface uplift is obtained when accounting for shear failure, and for a 'reasonable' overpressure greater than the tensile strength. (Note that this overpressure fits Equation (12) at the crest; $\sin(30)\,(\rho g D + T)$ *c.* 48 MPa). Unfortunately, the geometrical pattern of bedrock failure was not provided in this study.

From an engineering plasticity viewpoint

In engineering mechanics, a problem similar to a magmatic chamber is that of a pressurized cavity, applied to metal indentation and tunnelling. A technique known as slip-line field theory is used. For example, Nadai (1950) displayed the slip-lines solution associated with the indentation of an infinite plastic medium (Fig. 3a). Defining the radial and tangential normal principal stresses as σ_r and σ_θ and k as Tresca's yield stress, the plasticity condition reduces to $\sigma_r - \sigma_\theta = \pm 2k$ and solutions take the form:

$$\sigma_r = \pm 2k \ln\left(\frac{R}{r}\right), \quad \sigma_\theta = \pm 2k\left[1 + \ln\left(\frac{R}{r}\right)\right].$$

The resulting slip-lines are two orthogonal families of logarithmic spirals, commonly observed in steel plates pressed against a cylindrical stamp.

Prediction of plastic flow patterns for the even 'simpler' problem of flat indentation remains difficult because there are many possible slip systems. Closed-form kinematical solutions for flat indentation were calculated by Salençon (1969, Fig. 3b) and will be used further at the end of this paper. A lower bound for the internal pressure associated with failure around a cylindrical cavity was provided by Salençon (1966), whereas Caquot & Kerisel (1956) and d'Escatha & Mandel (1974) analysed the static admissible stress field for an upper bound using various friction and cohesion values. d'Escatha and Mandel presented graphical solutions based on the slip-line characteristics method (shown in Fig. 3c), and Caquot & Kerisel (1956) provided closed-form solutions. Fairhurst & Carranza-Tores (2002) used the numerical code Fast Lagrangian Analysis of Continuum (FLAC) to simulate a progressively decreasing support pressure on the wall

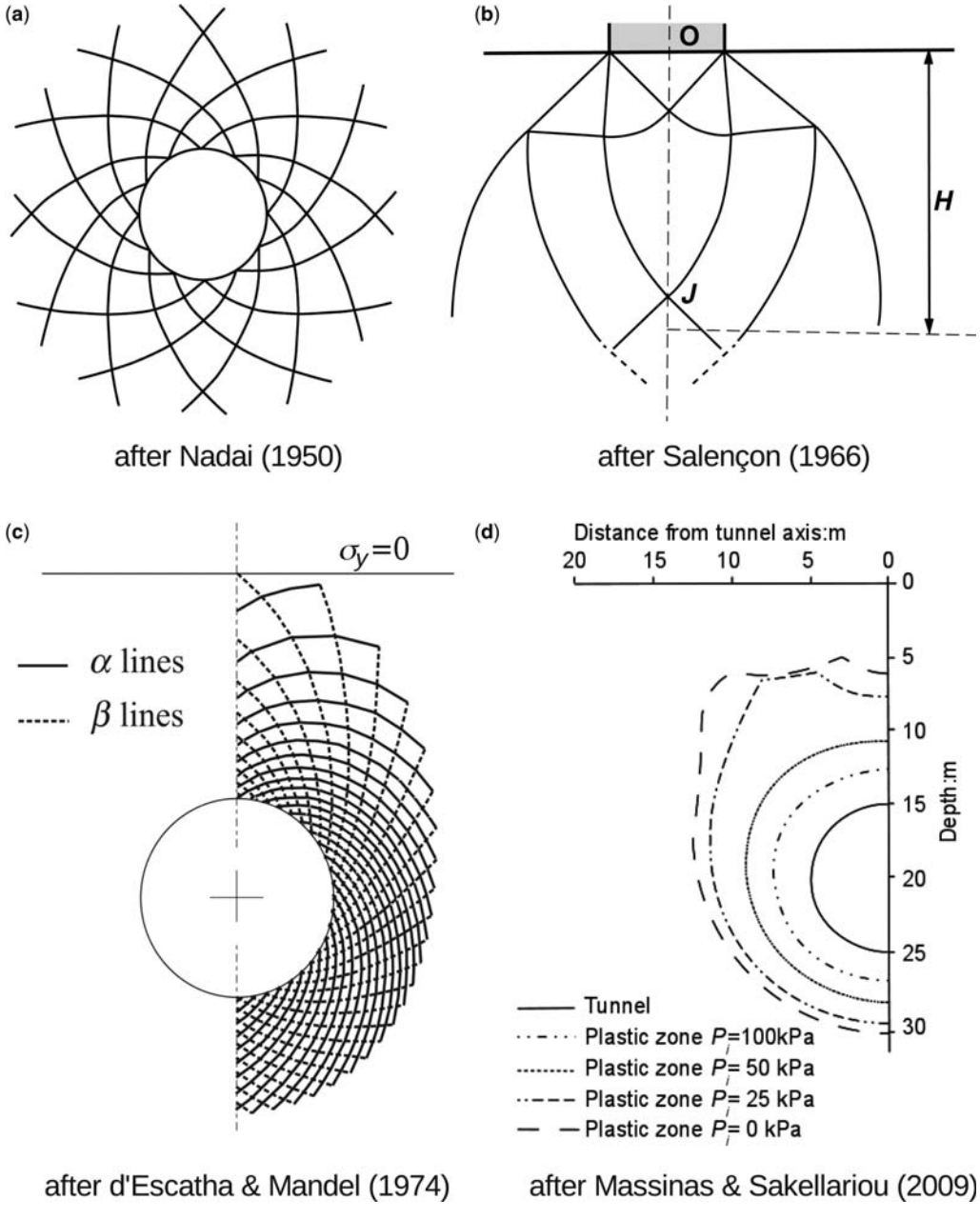

Fig. 3. Solutions from engineering mechanics. (**a**) Slip-line solution for circular indentation in a perfectly plastic infinite medium (after Nadai 1950, in which a photograph of steel indentation shows striking similarity). (**b**) Closed-form solution for flat indentation, displaying slip-line intersection at the axis of symmetry of flat indentation for $OJ/a > 5.298$ (after Salençon 1969). (**c**) Slip-line characteristics calculated by d'Escatha & Mandel (1974) for a friction angle $\varphi = 20^\circ$. (**d**) Plasticized domain calculated by Massinas & Sakellariou (2009) for different internal support pressures (P_i) in tunnels (note the ear shape appearing at some stage).

of a circular tunnel, and observed that failure did not start until the pressure was reduced to 80% of Caquot & Kerisel's (1956) upper bound value.

More recently, Massinas & Sakellariou (2009) provided another closed-form solution of the critical support pressure P_{cr} for wall failure around a tunnel.

Bipolar coordinates α and β were used similarly to that of Jeffery (1920), in which $\alpha_1 = \cosh^{-1}(H/R)$. Here, P_o is defined as the uniform external pressure (set as a proxy to the gravity load at the cavity's centre) and the Mohr–Coulomb friction angle φ is defined as before. Failure occurs at the wall for the minimum value of internal support pressure P_{cr}, which occurs when coordinate β equals 0 at the tunnel crest:

$$P_{cr} = \frac{P_o(1 - \sin\varphi)(1 + \sin^2\beta/\sinh^2\alpha_1) - T_o\sin\varphi}{1 + (1 - \sin\varphi)\sin^2\beta/\sinh^2\alpha_1}. \quad (13)$$

For $\varphi = 30^\circ$ and $\beta = 0$,

$$P_{cr} = \frac{P_o - T_o}{2}.$$

Note how this critical overpressure compares with that calculated in Equation (11): it is equal when considering (1) that signs are opposite for a depressed cavity and for an inflating chamber and (2) that the integrated average of a linearly increasing pressure with depth corresponds to half the maximum pressure P_o.

According to Massinas & Sakellariou (2009) and references therein, for deep tunnels with $H/R \geq 7$, the geometry of the plasticized domain is circular around the tunnel as the effect of the free surface is less than 10%. For shallow tunnels with $H/R < 7$, the geometry of the plasticized domain becomes eccentric (ear-shaped; Fig. 3d).

The role of pore-fluid pressure

The role of pore-fluid pressure in volcanic systems has long been thought to contribute to complex mechanisms such as heating of confined pore water by intrusions, degassing of intrusions, discharges of highly pressurized fluids from depth or deformation by faulting (e.g. Day 1996). Here, we will use a very simple assumption about the role of pore-fluid pressure in the bedrock, and argue how it can play a fundamental role in the mode of fracturing around magmatic chambers. Hubbert & Rubey (1959) proposed that fluids in pores produce an effective normal stress $\sigma_{eff} = \sigma_n - p_f$ that is represented in the Mohr–Coulomb yield criterion as:

$$\tau = S_o - (\sigma_n - p_f)\tan(\phi). \quad (14)$$

Hubbert & Rubey (1959) expressed p_f in terms of the vertical lithostatic stress and the pore-fluid pressure ratio λ, so that $p_f = -\lambda\rho g y$. In a rock of density 2500 kg m^{-3}, $\lambda = 0.4$ for hydrostatic pore-fluid pressure and $\lambda = 1$ for lithostatic pore-fluid pressure. While Townend & Zoback (2000) argued convincingly that hydrostatic pore-fluid pressure appropriately describes an equilibrium state within the crust, lithostatic pore-fluid pressure may also be relatively common in nature since many well data indicate values of $\lambda = 0.9$ (Engelder & Leftwich 1997; Hillis 2003). If we consider this extreme case of lithostatic pore-fluid pressure in the bedrock surrounding a magmatic chamber, then the component of gravity is cancelled out in the failure criterion (Equation (14)) and wall failure at the chamber wall can then be evaluated without accounting for this body force (Equation (5) becomes valid again).

If the development of up to lithostatic pore-fluid pressures in the neighbourhood of a magmatic chamber can be justified, then shear and tensile failure are predicted to occur under relatively small internal overpressures of the order of the tensile strength of rocks (10 MPa).

A state of lithostatic pore-fluid pressure surrounding magmatic chambers should therefore be envisaged when field observations report a majority of mode I opening dykes (e.g. Gudmundsson 2006). This point will be further discussed in the Conclusion.

Numerical modelling of inflating magma chambers

Numerical method and set-up

The finite-differences code Parovoz is used (Poliakov & Podladchikov 1992; Podladchikov *et al.* 1993), which is based on the FLAC method (Cundall & Board 1988). In this method the equations of motion are solved explicitly in time and in large-strain mode, retaining a locally small strain formulation commonly used in continuum mechanics. This method is well known for being able to reproduce the initiation and propagation of non-predefined faults (treated as shear bands, e.g. Poliakov & Podladchikov 1992), and it has been used in a number of geodynamical settings (e.g. Burov & Guillou-Frottier 1999; Gerbault *et al.* 1998; Burov *et al.* 2003; Lavier *et al.* 2000). The program executes the following procedure in one time-step. Velocities are first calculated from the equation of motion with density ρ, time t, velocity vector V, stress tensor σ and gravitational acceleration g:

$$\rho\frac{dV_i}{dt} + \frac{d\sigma_{ij}}{dx_i} = \rho g \quad (15)$$

where d/dt and d/dx_i are the time and space derivatives. The deformation rate is:

$$\varepsilon_{ij} = \frac{1}{2}\left(\frac{dV_i}{dx_j} + \frac{dV_j}{dx_i}\right) \quad (16)$$

and is used to calculate the new stress distribution from the elasto-plastic constitutive law. From these new stresses, nodal forces and displacements are evaluated and inserted in the next time-step. Elasticity relates stress and strain using the Lamé parameters λ and G (δ_{ij} is the Kroenecker symbol):

$$\sigma_{ij} = \lambda\varepsilon_{ij} + 2G\varepsilon_{ij}\delta_{ij}. \quad (17)$$

Non-associated plastic flow is modelled (e.g. Cundall 1989; Gerbault *et al.* 1998; Kaus 2010) with a frictional Mohr–Coulomb stress criteria given in Equation (10) and a dilatancy set to 0 (Vermeer & de Borst 1984). Common failure parameters are chosen with friction $\varphi = 30^\circ$, cohesion $S_0 = 10$ MPa and tensile cut-off strength $T = 5$ MPa. Modelled shear bands are commonly assimilated to shear 'faults'. Tensile failure is detected when one or more stress components exceeds the tensile cut-off T. Despite Parovoz being a two-dimensional plane-strain code, the condition for failure is evaluated with the three stress components. Although Parovoz can identify domains of tensile failure, the mesh continuum cannot split such as in real mode I crack opening. However, White *et al.* (2004) successively compared domains of tensile failure identified by FLAC^{2D}, with a Particle Flow Code that can track individual microfractures via breakable bonds.

Our problem is modelled in plane-strain. The left border ($X = 0$) represents the vertical axis of symmetry passing through the centre of a circular magma chamber. Domain dimensions are 100 km in length and 80 km in depth, far enough from the zone of interest to minimize border effects. The chamber has radius $R = 2$ km and is located at $H = 7$ km depth.

The mesh is defined with quadrilateral elements of height and width equal to 25 m over the first 12 km of the model domain. Grid resolution progressively reduces in both directions to *c.* 1 km at the bottom-right corner. The total number of mesh elements is 275,000.

In the model, all borders apart from the free ground surface have free-slip boundary conditions. A uniform rock density is set at $\rho = 2500$ kg m^{-3} (Table 1 summarizes all analytical and numerical

Table 1. *List of parameters and specific values used for the reference model*

Symbol	Description	Value
R	Radius of chamber	2 km
H	Depth to centre of chamber	7 km
D	Depth to crest of chamber, used by Grosfils (2007) $H-R$	5 km
G	Shear modulus: bedrock, chamber	20 GPa, 2 GPa
ν	Poisson's ratio	0.25
ρ	Density	2500 kg m^{-3}
g	Gravity	9.81 m^2 s^{-1}
α	Angle between vertical axis and line at surface origin to any point at wall, used by Jefferys (1920)	
θ	Angle between horizontal axis at centre of chamber and any point at wall, used by Grosfils (2007)	
σ_{xx}	Horizontal stress	
$\sigma_{\theta\theta}$	Hoop stress at the chamber wall	
C	Free surface factor : $1 + 2\tan\alpha''$, used by Grosfils (2007)	
φ	Bedrock friction angle	30°
S_o	Bedrock cohesion	10 MPa
T_o	Bedrock tension deduced from S_o	17.3 MPa
T	Bedrock cut-off tensile strength	5 MPa
P, σ_{II}	First and second stress invariants	
τ, σ_n	Tangential and normal stress along any given plane	
ΔP	Internal overpressure	
ΔP_S	Critical overpressure for tensile failure at the surface	Equation (4)
ΔP_T	Critical overpressure for tensile failure predicted from common studies, neglecting gravity	Equation (5)
ΔP_{TG}	Critical overpressure for tensile failure predicted by Grosfils (2007)	Equation (7)
ΔP_{MC}, ΔP_{MCS}	Critical overpressure for shear failure predicted in this study	Equations (11), (12)
P_o, P_{cr}	Uniform external pressure, and critical internal overpressure defined by Massinas & Sakellariou (2009)	Equation (13)
ΔP_1, ΔP_2, ΔP_3	Modelled internal overpressure at different stages of failure	
λ	Pore pressure ratio	0/1
p_f	Pore-fluid pressure	

variables). The model is initially set up with isotropic lithostatic components (weight of overburden rocks) so that a strain of only 1‰ develops during readjustment to the plane-strain conditions (e.g. Turcotte & Schubert 1982).

Numerical benchmarks of the results that are described in the following sections are included in the Supplementary Material. The formation and development of precise shear bands is conditioned by a sufficiently high mesh resolution, which requires computationally expensive runs. The major numerical concern is mesh-locking effects as shear bands form and propagate from the chamber wall. The finite element code Adeli (Hassani *et al.* 1997; Chery *et al.* 2001) is used to benchmark our solutions. The benchmark shows the effects of meshed versus unmeshed chamber and of coarse mesh resolution, especially when the domain becomes highly plasticized. Localizing plastic deformation is known to be complicated to model numerically (e.g. Yarushina *et al.* 2010); a research objective could therefore be to improve this benchmark with high-resolution models, similar perhaps to those that have been conducted for the problem of fault propagation in accretionary prisms (Buiter *et al.* 2008).

Assumptions about the rheological behaviour of the chamber

Many models of an inflating magmatic chamber do not include the internal domain of the magmatic chamber in their mesh. However, this has been included here in order to achieve high mesh resolution with the quadrilateral elements formulation of Parovoz. The rheology of the chamber must therefore be defined using Lamé parameters. While a magmatic chamber filled with low-viscosity fluid should be assumed incompressible (Poisson's ratio = 0.5), many studies point to the important proportion of volatile phases which reduce both its elastic rigidity and its incompressibility (Bower & Woods 1997; Huppert & Wood 2002; Rivalta & Segall 2008). The effects of the elastic properties of the chamber were therefore verified. The greater the internal Young's Modulus the more the chamber dilates and 'absorbs' its internal pressure, thus transferring less pressure to the outer walls and bedrock domain. The pressure felt out of the chamber walls is best measured via the second invariant of the deviatoric shear stress, similar to the approach used by Chery *et al.* (1991).

If the Young's Modulus is reduced to 10 times that of the external bedrock, then more than 90% of the applied internal pressure is transferred to the outer domain. In this case, the value of Poisson's ratio does not act significantly. The tests show that modelled stress and deformation become indistinguishable for models with $\nu = 0.25$ and $\nu = 0.45$. The presented reference model assumes Lamé parameters equal to $1/20$ those outside the chamber (corresponding to $\nu = 0.25$ and $E = 2.5$ GPa, whereas in the bedrock $E = 50$ GPa).

Numerical experiments follow a procedure in which the internal overpressure (ΔP) increases progressively. This pressure increase occurs proportionally to the time-step of the model, according to $\Delta P = A \times$ time where A is a coefficient fixed so that the pressure increases (1) fast enough for the total computing time of the run to be reasonable and (2) slow enough so that deformation resulting from a specific ΔP detected during our sampling frequency provides a quasi-static solution. Application of an internal overpressure that overshoots the yield strength of elements can lead to numerical inconsistencies. This justifies the application of a continuous radial deformation to model magmatic inflation (e.g. Chery *et al.* 1991). However, for the specific purposes of our study, application of a radial overpressure is more appropriate (as in tunnelling engineering, see above).

In the real world, the onset of an eruption or dyke injection releases confined magmatic fluids from the chamber, inhibiting further increase in internal overpressure. However, Wegler *et al.* (2006) interpreted continuously increasing shear wave velocities below the Merapi volcano as an indicator of increasing magmatic pressure in between two consecutive eruptions in 1998. The application of an elevated internal overpressure in our models should therefore be considered within the context of rapid arrival of over-pressurized magma and as a preliminary stage of regional microcracking and damaging of the host rock, prior to the onset of dyke injection or magmatic eruption (see Discussion section).

Different stages of deformation with increasing pressure

Sequential results of a reference model (M1 in Table 2) are presented (Fig. 4) at increasing internal overpressure. Zones of failure, shear strain, deviatoric and horizontal stresses are described below for three different stages of evolution.

Stage 1: Development of surface tensile failure (ΔP_1)

Internal overpressure increases progressively from an initial uniform lithostatic state. Tensile failure is first reached at the origin X_o on the ground surface, and expands progressively both in width and depth. Since this surface is defined as stress free, failure is only limited by the equality of σ_{xx} with the tensile strength $T = 5$ MPa. Locally, the

Table 2. *Numerical models. Initial conditions are distinguished according to the magmatic chamber being included or not in the mesh, pore-fluid pressure (hydrostatic or lithostatic), tensile strength* T *(elastic means the entire bedrock is elastic as opposed to elasto-plastic) and applied overpressure* ΔP

Model name	Process name	Fig.	Chamber (GPa)	Fluid pressure	T (MPa)	Pressure ΔP (MPa)	Fracturing stage	Surface uplift (m)
M1	M3dpten5b	4a	$\lambda = \mu = 1$	–	5	54	1-surface	1.5
		4b				114	2-wall	4.1
		4c				127	3-connection	5.5
		4d				135	3-connection	6.7
M2	M3dpten5L1	6a	$\lambda = \mu = 1$	Hydrostatic	5	55	2-wall	1.5
M3	M3dpcten5L3	6b	$\lambda = \mu = 1$	Lithostatic	5	20	2-wall	0.5
M4	M3dpR3L3a	6c	$\lambda = \mu = 1$	Lithostatic	17.3	20	3-connection	1.0
A1a	M3f50r3	A1	$\lambda = \mu = 1$	–	17.3	50	1-surface	2.06
A1b	M3cp50elas	A1	$\lambda = \mu = 1$	–	Elastic	50	Elastic	2.05
A1c	bull9	A1	Empty	–	17.3	50	1-surface	2.13
A1d	bull9elas	A1	Empty	–	Elastic	50	Elastic	2.13
A2a	M3cp120	A2	$\lambda = \mu = 1$	–	17.3	120	2-wall	4.9
A2b	M3cp120elas	A2	$\lambda = \mu = 1$	–	Elastic	120	2-wall	5.11
A2c	bull9	A2	Empty	–	17.3	120	2-wall	5.12
A2d	bull9elas	A2	Empty	–	Elastic	120	2-wall	5.25
A3a	M3cp20nog	A3	$\lambda = \mu = 1$	–	17.3	15.2	2-wall	1.08
A3b	bull9nog	A3	Empty	–	17.3	15.2	2-wall	1.18
A3c	M3dpcL3	A3	$\lambda = \mu = 1$	Lithostatic	17.3	18.1	2-wall	1.15
A3d	bull8nog	A3	Empty	–	17.3	18.8	2-wall	2.5

Results are summarized in terms of stage of fracturing and amount of surface uplift. Models A1a–A3d are displayed in the Supplementary Material.

horizontal stress is slightly higher with $\sigma_{xx} = 6$ MPa because of values taken at the centre of 25 m-thick mesh elements.

The analytical prediction (Equation (4)) without gravity provides failure at the surface for $\Delta P_1 = T(H^2 - R^2)/2R^2 = 28.13$ MPa. The numerical model produces surface rupture for $27.4 < \Delta P_1 < 28.4$ MPa (numerical time-step sampling is automatic and cannot correspond to exact critical analytical pressures). The consistency of the numerical value of ΔP_1 with the analytical solution of Equation (4) indicates that failure at the surface is less dependent on the gravitational load acting on the system than on the local state of stress at the very top surface where gravity stresses vanish.

Stage 2: Development of shear failure along the chamber wall (ΔP$_2$*)*

As internal overpressure continues to increase, tensile failure ceases to propagate and is replaced by normal shear faults that also propagate downwards. Shear failure then initiates around the chamber (Fig. 4b). The numerical model indicates that this occurs at an overpressure of 70 MPa, in excellent agreement with the Mohr–Coulomb yield prediction evaluated in Equation (11): $\Delta P_{MC} = (-\rho g y + T_o) \sin \varphi = 71$ MPa.

Shear failure first initiates in the upper quarter of the chamber wall, consistent with analytical predictions and Figure 2. With increasing overpressure, shear bands initiating at the chamber wall are oriented at an angle $45 \pm \varphi/2 = 30^\circ$ to the most compressive radial direction, in agreement with expectations for a non-associative Mohr–Coulomb material (e.g. Vermeer & de Borst 1984; Kaus 2010). These shear bands develop eccentrically from the chamber, and cross each other at an angle of 60° consistent with a friction angle $\phi = 30^\circ$ (e.g. d'Escatha & Mandel 1974; Vermeer & de Borst 1984; Gerbault *et al.* 1998). Note that the difference in orientation between these modelled shear bands and those calculated by d'Escatha &

Fig. 4. Reference model M1 for different stages of increasing internal pressure (ΔP), tensile strength $T = 5$ MPa. (**a**) Stage 1: tensile failure initiates at the surface when $\Delta P_1 = 28$ MPa, later forming inward-dipping normal faults. (**b**) Stage 2: shear failure initiates around the chamber walls from $\Delta P_2 = 70$ MPa, and forms an eccentric fault pattern here shown at $\Delta P = 100$ MPa. (**c**) Stage 3: Both fault systems connect at $\Delta P_3 = 130$ MPa. (**d**) The fault system expands, forming a vertical fault pattern from the chamber to the surface. Figures show (from left to right) rupture zones in blue, the 2nd invariant of the cumulated deviatoric shear strain and the 2nd invariant of the stress tensor.

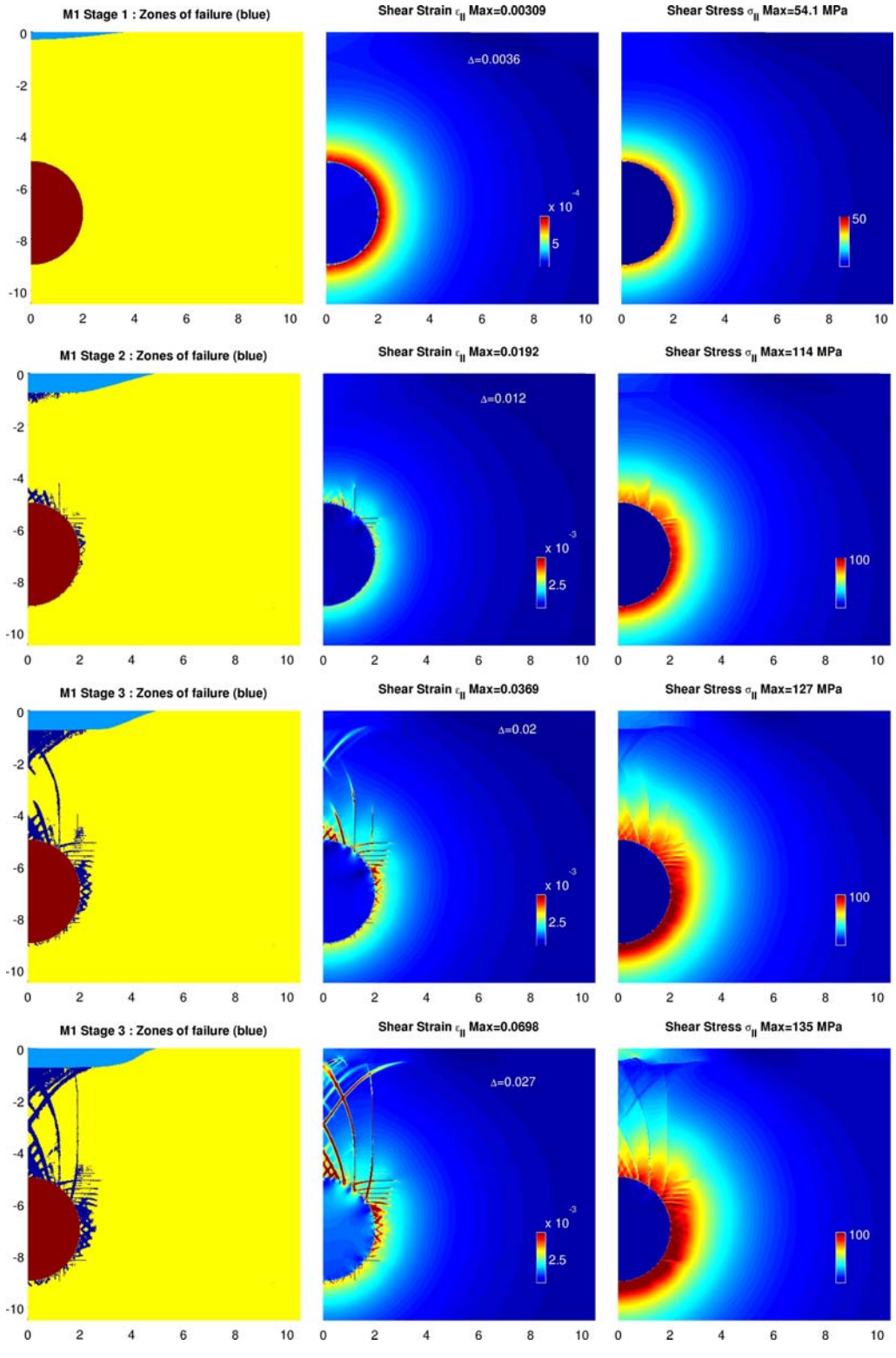

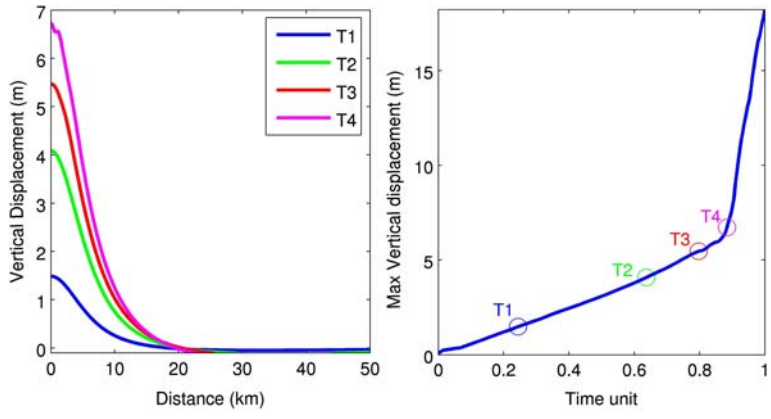

Fig. 5. Surface displacements from model M1 at different times T1, T2 and T3 corresponding to stages illustrated in Figure 4. Vertical displacement is shown as a function of distance (left) and as a function of time (right). Note departure from linear increase at T3, when the failure pattern connects the chamber to the surface.

Mandel (1974, friction angle $\varphi = 20^\circ$, Fig. 2) stems from perpendicularly orientated principal compressive stresses due to the application of either an overpressure (this study) or an underpressure (d'Escatha & Mandel 1974).

Stage 3: Faults connection and possible secondary chamber (ΔP_3)

With increasing overpressure, outward-dipping shear and reverse faults expand from the chamber upwards simultaneously with inward-dipping normal faults that propagate from the surface downwards. These two plasticized (i.e. faulted) domains eventually connect and merge (Fig. 4c). The connection occurs at a depth d_m along the vertical axis of symmetry as a function of the chamber width and depth (R and H). This depth d_m compares with a typical distance at which slip-lines cross each other in analytical solutions for flat indentation of a perfectly plastic material (Salençon 1966, distance OJ, Fig. 2b). We return to this point in the Discussion and speculate that this local dilation zone, where deep and shallow shear zones connect, may focus a secondary magmatic reservoir close to the surface.

This third stage where the domains of plasticized material connect the chamber to the surface occurs when ΔP reaches about 130 MPa in the model. The possibility of achieving such a high overpressure seems extreme in a quasi-static situation; such high overpressures may however occur as a transient phenomenon if extremely rapid arrival of overpressurized magmatic fluids, which have no time to relax within the chamber, is considered.

Whereas failure at the chamber wall initiates over the crest domain, consistent with analytical predictions illustrated in Figure 2, most active shear bands depart from the chamber wall at the angle interval θ *c.* 45–60° from the horizontal direction taken at the chamber centre. Our explanation for a greatest intensity of localized deformation at this location is the following. Above the crest of the chamber, principal stresses rotate by 90°. Shear bands that propagate to the surface must also rotate, cross each other and reflect on the vertical axis of symmetry. Instead, at θ *c.* 45–60° changes in stress orientations are minimal in the domain between the chamber wall and the top surface; this favours the formation of straight shear bands expanding from the chamber to the surface, which eventually form at the final stage of the model (Fig. 3d). The geometry of failure therefore results from a dynamic mechanism of deformation that minimizes work between the chamber and the surface, rather than depending solely upon the local stress minima (e.g. Masek & Duncan (1998) applied the minimum work principle to mountain building). In addition, note that shear bands initiating at θ *c.* 60° at the chamber wall also form at 30° from the most compressive stress (radial), and are thus naturally oriented at $60 + 30 = 90^\circ$ (i.e. the vertical) and closely parallel to the 'fabric' of the mesh.

When plotting surface displacements at different time-steps (Fig. 5a) and also as a function of time (Fig. 5b), departure from a linear elastic increase in surface uplift is seen to become significant after Stage 3 when the failure domain is connected from the chamber to the surface.

The effect of fluid pressure on bedrock deformation

It was argued analytically above that the presence of pore-fluid pressure p_f would enable failure for

significantly lower internal overpressures because it annihilates the gravity component in the yield stress criterion. This effect is now illustrated with numerical models by taking into account pore-fluid pressure in the yield stress criterion.

Two sets of models are performed using Parovoz in which the yield criterion is expressed according to Equation (14), with a constant bedrock pore-fluid pressure set first to hydrostatic ($\lambda = 0.4$) and then to lithostatic ($\lambda = 1$) pressure.

When accounting for a hydrostatic pore-fluid pressure ($p_f = \rho_w g y$; $\lambda = 0.4$) in the bedrock, the progressive increase in internal overpressure leads to a first stage of tensile and normal faulting at the surface followed by the initiation of shear failure at the chamber wall (Stage 2) at an overpressure consistent with the analytical prediction $\Delta P_{MC} = \sin\varphi(T + (\rho_r - \rho_w)gD) = 43$ MPa. Figure 6a displays a snapshot of this model at 54 MPa, where the initiation of shear failure at the chamber wall can be observed (blue dots).

When accounting for a lithostatic fluid pressure ($p_f = \rho_r g y$, $\lambda = 1$) in the bedrock, the onset of wall shear failure is predicted when $\Delta P_{MC} = \sin\varphi\ T_o$ according to Equation (11). Thus, if tensile strength $T = T_o = S_o/\tan\varphi = 17.3$ MPa (there is no cut-off), then $\Delta P_{MC} = 8.6$ MPa. The onset of wall tensile failure is predicted from Equation (5) when overpressure $\Delta P_T = T(H^2 - R^2)/H^2$. In the case where the tensile strength $T = 17.3$ MPa, tensile failure therefore cannot occur since $\Delta P_T = 15.9$ MPa which is greater than ΔP_{MC}. However, if tensile strength $T = 5$ MPa, tensile failure is predicted at the wall for $\Delta P_T = 4.6$ MPa which is lower than ΔP_{MC}.

The numerical results are consistent with these predictions. With a tensile strength cut-off $T = 5$ MPa, the numerical model produces tensile failure at the wall and before any failure occurs at the ground surface (Fig. 6b). The plasticized domain has an almost circular shape; a subsequent increase in internal pressure increases its radius, with connection with the surface taking the shape of an amphora (not shown). ΔP needs to reach 21 MPa so that the plastic domain branches to the surface.

Another model is displayed in Figure 6c, in which the bedrock is again assumed to be at lithostatic pore-fluid pressure but for which there is no prescribed tensile strength cut-off (therefore $T = T_o = S_o/\tan\varphi = 17.3$ MPa). In this case, shear failure is shown to develop throughout the bedrock with a precise onset at the wall when $\Delta P = 8.6$ MPa (as predicted above).

Table 2 lists the fracturing stages and values of surface uplift for these models with hydrostatic and lithostatic pore-fluid pressure and shows that, for internal pressures equivalent to model M1, the fracturing pattern occurs systematically a stage ahead and is associated with greater deformation than in model M1.

Discussion of the models with respect to geological observations

Shear fracturing around exposed intrusions, open faults and fluids

Many field observations report mode I opening structures (mainly dyke intrusions) as a dominant process of deformation outside magmatic bodies (e.g. Gudmundsson 2006; Holohan *et al.* 2009). However, geological studies also report shear faulting prior to dyke intrusion. Figure 7 illustrates such observed shear structures.

The Solitario Laccolith, Trans-Pecos Texas, is a 16 km diameter dome that displays a complex sequence of doming with sill and dyke intrusions that were mapped and dated by Henry *et al.* (1997). They interpreted quartz-phyric rhyolite dykes (their Tir4) to have intruded along radial and concentric shear fractures during doming (Fig. 7a).

The island of Arran, Scotland, is a typical reference for preserved structures formed during magmatic intrusion (Fig. 7b). Describing these, Woodcock & Underhill (1987) note how 'late in the intrusion history of the Paleocene Northern granite, the major faults (in Permian–Triassic New Red Sandstones) on the southeast side of the granite formed a conjugate strike-slip system that accommodated radial expansion of the pluton'.

A 30 cm-scale rock is displayed in Figure 7c, which was sampled along the track of the Glen Rosa valley in Arran. The grey part of this rock (the 'bedrock') displays a regular pattern of conjugate shear bands crossing each other at *c.* 60°, adjacent to another unfaulted domain of whiter colour (presumably the 'fluid'). One of these shear bands (A) has been infiltrated by that fluid, and is about 2 mm thick. About 20 cm to the right, another much thicker (*c.* 2 cm) limb of fluid expands through the bedrock and overprints the conjugate system of faults (B). This observation may be interpreted as follows. First, shear fracturing has developed pervasively in the bedrock surrounding an over-pressurized medium (which did not fail). The fluid then infiltrated the shear bands, prior to or simultaneous with a more massive event in which tensile opening expelled greater amounts of fluid throughout the bedrock.

Other independent observations argue in favour of the occurrence of shear fracturing around magmatic chambers. First, in a general context of extension excluding fluid involvement, it is well known that tensile stress does not systematically lead to mode I opening. For example, Ramsey & Chester

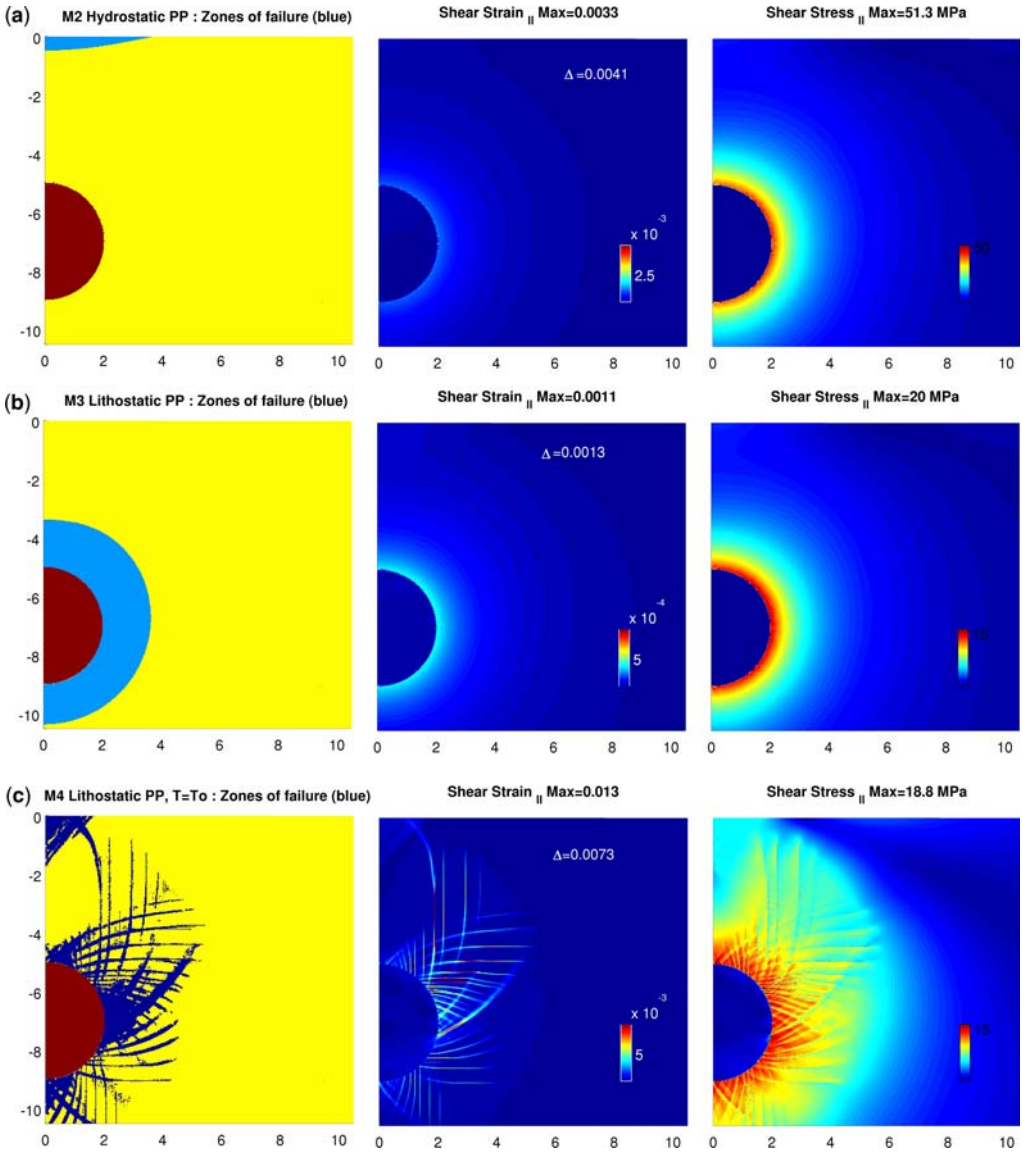

Fig. 6. Models accounting for an effective pore-fluid pressure in the host rock. (**a**) Hydrostatic pore pressure, tensile strength $T = 5$ MPa for $\Delta P = 54$ MPa. Tensile failure develops at the top surface and shear failure occurs at the wall (dark blue dots). (**b**) Lithostatic pore pressure, tensile strength $T = 5$ MPa for $\Delta P = 20$ MPa. Tensile failure develops all around the chamber wall. (**c**) Lithostatic pore pressure with no tensile strength cut-off ($T = T_o = 17.3$ MPa) at $\Delta P = 20$ MPa. Shear failure develops everywhere in the bedrock.

(2004) showed from laboratory experiments under triaxial tension, that rock failure can evolve continuously from mode I opening cracks to mode II shear fractures as the confining pressure increases. Second, the observation of seismicity under volcanic edifices indicates double-couple earthquake focal mechanisms, associated with or prior to an eruption (e.g. Waite & Smith 2002; Kumagai *et al.* 2011). Double-couple focal mechanisms are an indicator for failure occurring in mode II, independently of the recognized presence of large amounts of fluids in active volcanic zones.

The present analytical and numerical study indicates that the occurrence of mode I fracturing

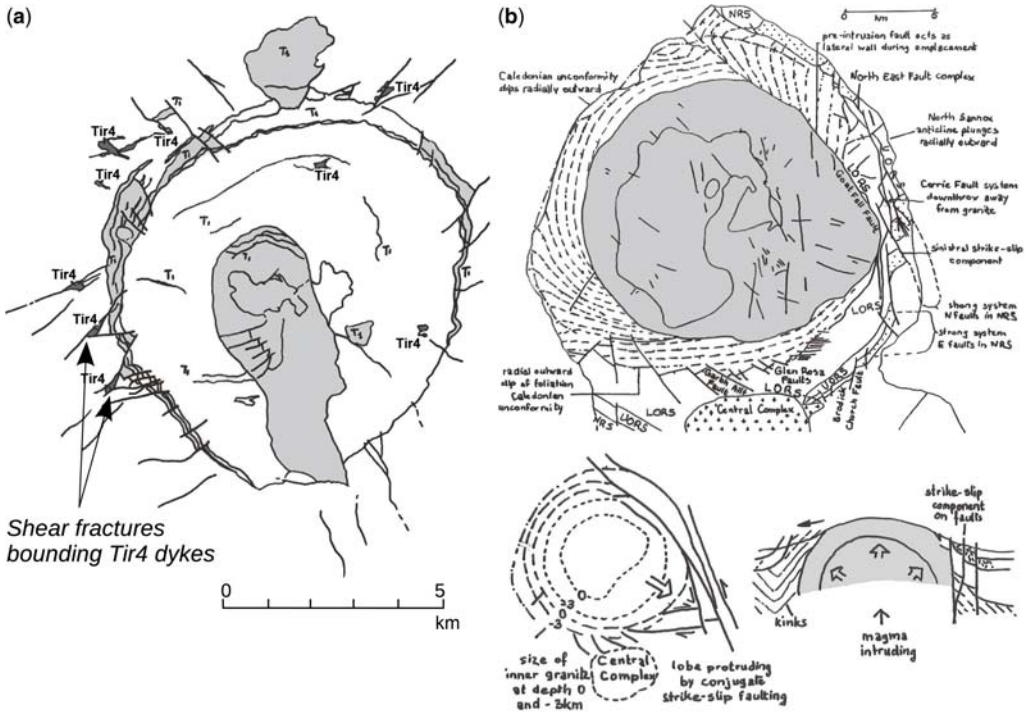

Solitario Laccolith, Texas (after Henry *et al*. 1997)

Arran Northern granite, structural map and interpreted map and section views (after Woodcock & Underhill 1987)

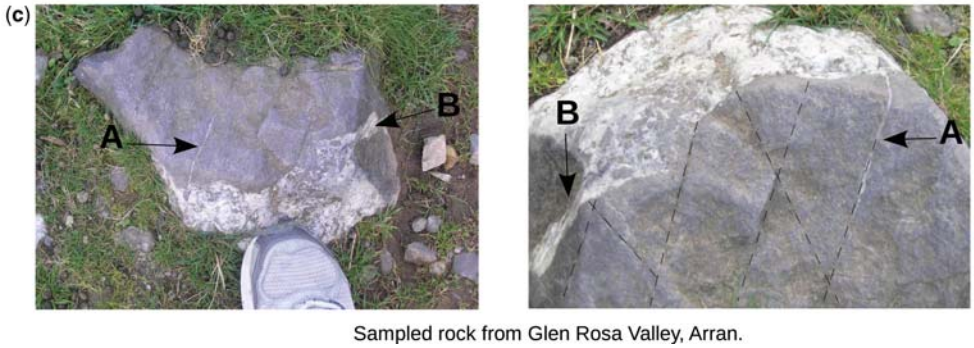

Sampled rock from Glen Rosa Valley, Arran.

Fig. 7. Field examples of shear fractures around magmatic bodies. (**a**) The Solitario lacccolith, Texas, showing dyke intrusions bounded by pre-existing shear faults (simplified after Henry *et al.* 1997). (**b**) Geological structural map of Isle of Arran, Scotland, with interpreted map and plane views of structures forming during pluton ascent, after Woodcock & Underhill (1987). (**c**) Rock sampled at Isle of Arran in the Glen Rosa valley, displaying a conjugate fracture pattern along which fluid penetration occurs at location A and a non-oriented more massive intrusion at location B.

around an inflating magmatic chamber requires that the bedrock medium contains sufficient pore-fluid pressures close to a lithostatic state. It suggests that once the bedrock around an inflating chamber is sufficiently weakened by either processes of shear fracturing, microcracking or transport of fluids in pores associated with the inflation, the subsequent massive stage of mode I fracturing can occur by means of dyke or sill emplacement and eruption. A more complex dynamic model accounting for double-phase hydro-mechanical processes is required to demonstrate the validity of such mechanisms.

Insights from the modelled failure geometry

The sophisticated faulting geometries obtained in the numerical experiments (stage 2 to stage 3) result from the complex stress pattern produced by the circular overpressure, and was achieved due to an uncommonly high numerical mesh resolution; no previously published numerical studies demonstrate such shear band geometries (to the author's knowledge).

When gravity is neglected (or when lithostatic fluid pressures are present), the geometry of the modelled shear bands is similar to slip-line solutions predicted by circular plane-strain indentation and displays logarithmic eccentricity (Nadai 1950; Fig. 3a). When gravity is accounted for, numerical results show strong similarities to slip-line characteristics around a collapsing tunnel by d'Escatha & Mandel (1974, Fig. 3c).

An interesting comparison with flat indentation can also be made. Salençon (1969) showed that the maximum distance $d_m = OJ$ from the indenter (at which slip-lines would cross each other along the central axis of symmetry before reaching the opposite free surface) satisfies a maximum height to width ratio $d_m/a = 5.298$ (where a is the half-width of the indenter and J is slip-line intersection point beyond which triangular block motion links with the opposite surface; Fig. 3b). Such a local zone of dilation due to crossing shear zones has previously been applied in the field of Earth Sciences in order to explain the development of tensile structures in compressional tectonic regimes. For instance, Lake Baikal results from the indentation of Asia by India (e.g. Tapponnier & Molnar 1976) and the Eifel volcanic zone is a result of the Alpine–European indentation (Regenauer & Petit 1997). Salençon's relationship ($H > 5.3\ R$ approximately) may be invoked to a first order to assess whether a magmatic chamber is deep enough to generate a secondary magmatic reservoir very close to the surface. This speculative process requires a systematic investigation of double sources below volcanoes worldwide (e.g. below Askja, Sturkell

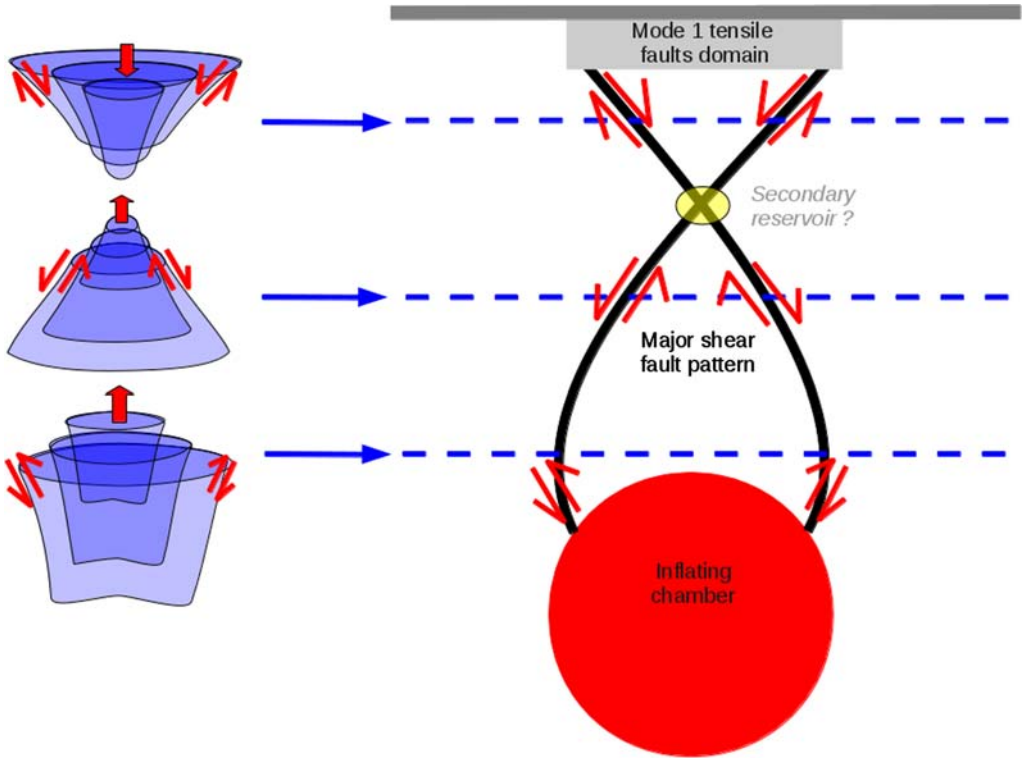

Fig. 8. Diagram of failure patterns from the surface to the top of a circular pluton, displaying the imbrications of individual faulted blocks for different depths. A zone of dilation forms locally at the crossing point between upwards- and downwards-propagating shear zones, suggesting the formation of a secondary magmatic reservoir (compare to Fig. 3b).

et al. 2006; below la Soufrière, Foroozan *et al.* 2010; and below Tungurahua, Ruiz *et al.* 2010).

Structurally, the present modelled shear band structures dip inwards when initiating from the ground surface and dip outwards when initiating from the chamber wall. Despite the similarity, these geometrical results remain difficult to compare to numerical and analogue studies that consider deflation instead of inflation (e.g. Roche & Druitt 2001; Kusumoto & Takemura 2003; Acocella *et al.* 2004; Acocella 2007). Figure 8 depicts our modelled geometries and relates them to structures likely observable in the field, with different depths corresponding to different levels of surface erosion and exhumation. Different imbricated structures appear. At the surface, and possibly coeval with tensile cracks, normal faults form cones imbricated one into the other downwards; close to the chamber, reverse faults develop like imbricated flower pots. At intermediate depths, upwards-open cones and previous imbricated cones may coexist simultaneously and overlap as deformation progresses. Such geometries are best found in the field in relatively old and well-preserved plutonic and annular intrusive complexes, for which relatively slow ascent and cooling would maintain the structures deforming around them (e.g. Woodcock & Underhill 1987; Maza *et al.* 1998; Lafrance & John 2001). Clearly, a thorough investigation of natural analogues is needed to demonstrate the validity of these structural geometries.

Conclusion

In studying the stress conditions for failure around a spherical magma chamber subjected to an internal overpressure, assuming an elasto-plastic bedrock and a simple approximation of pore-fluid pressure, the following points have been demonstrated.

Failure occurs in shear mode along the chamber walls and for an internal overpressure (in excess of the state of lithostatic equilibrium) about half an order of magnitude (depending on the radius-to-depth ratio) greater than the usually inferred limit given by tensile strength of the rocks. The important role of the wall-parallel component of the lithostatic stress on failure conditions (Grosfils 2007) is therefore confirmed. It has also been shown that a chamber wall should fail in shear mode rather than in tensile mode, a common behaviour also assumed in tunnelling engineering mechanics (e.g. Massinas & Sakellariou 2009).

Only in the specific case where the bedrock is at a state of lithostatic pore-fluid pressure does tensile failure occur around the chamber for an internal overpressure close to the tensile strength (5–10 MPa). Consequently, if the bedrock surrounding an active volcano contains less than lithostatic pore-fluid pressures, then researchers investigating geodetic studies that use the Mogi solutions to infer chamber depth and radius should not be surprised to achieve their data fit with associated 'high' overpressures. In addition, ground surface deformation rapidly exceeds elastic solutions as soon as the failure domain connects the chamber to the surface.

The exceptionally precise geometries of the modelled shear bands were obtained due to a high mesh resolution, but these results should be confirmed with future benchmarks (Gerbault *et al.* 2012). These high-resolution shear bands are comparable to slip-line plasticity solutions in displaying eccentric structures and suggest that an initially deep magmatic chamber may generate a secondary reservoir closer to the surface, at the locus of intersection of major shear zones along the vertical axis of symmetry. Further systematic documentation of double reservoirs in magmatic systems is needed to confirm this scenario.

Naturally, all these results are valid in the context of an ideally circular magmatic chamber in a homogeneous, isotropic, elasto-plastic medium. A finger- or dyke-shaped intrusion would be better modelled with the crack theory, sensitive to the host rock tensile strength. As mentioned by Marti *et al.* (2008) or modelled by McLeod & Tait (1999), dyke intrusion may significantly affect the conditions for fault nucleation and propagation; the applicability of our model results is obviously limited to the circular geometry of the chamber. In addition, deformation is also governed by the rheology of the magma, temperature and viscosity of the bedrock, the driving pressure, stresses resulting from the intrusion itself, dynamic fluid transport through the chamber and the bedrock and many other temporally and spatially variable factors discussed elsewhere in the literature (e.g. Anderson 1936; Rubin & Pollard 1987; Lister & Kerr 1991; Rubin 1995; Day 1996; Fialko *et al.* 2001; Hurwitz *et al.* 2009; Karlstrom *et al.* 2010; Gressier *et al.* 2010; Galgana *et al.* 2011; de Saint Blanquat *et al.* 2011). Future research goals include the improvement of coupled hydromechanics modelling (Gerbault *et al.* 2012), the study of deflating conditions and the adaptation of these models to real volcanoes.

Thank are due to R. Hassani, J. Salençon and M. Sakellariou for sharing their knowledge on mechanics and O. Roche, V. Cayol, D. Healy, S. Holford, B. Mercier Lepinay, R. Plateaux and C. Ganino for sharing their knowledge on magmatic chambers. J. Giannetti provided priceless library support and J. Trevisan helped with the drawings. N. Croiset co-explored preliminary models and her work is acknowledged (Masters report, ENS Lyon, 2007). A detailed and enriching review by E. Grosfils improved the manuscript significantly.

References

Acocella, V. 2007. Understanding caldera structure and development: an overview of analogue models compared to natural calderas. *Earth Sciences Reviews*, **85**, 125–160.

Acocella, V., Funiciello, R., Marotta, E., Orsi, G. & de Vita, S. 2004. The role of extensional structures on experimental calderas and resurgence. *Journal of Volcanology and Geothermal Research*, **129**, 199–217.

Anderson, E. M. 1936. The dynamics of formation of cone-sheets, ring-dykes and cauldron-subsidences. *Proceedings of the Royal Society, Edinburgh*, **56**, 128–163.

Bonafede, M. & Ferrari, C. 2009. Analytical models of deformation and residual gravity changes due to a Mogi source in a viscoelastic medium. *Tectonophysics*, **471**, 4–13.

Bonafede, M., Dragoni, M. & Quareni, F. 1986. Displacement and stress fields produced by a centre of dilation and by a pressure source in a viscoelastic half-space: application to the study of ground deforma tion and seismic activity at Campi Flegrei, Italy. *Geophysical Journal of the Royal Astronomy Society*, **87**, 455–485.

Bower, S. M. & Woods, A. W. 1997. Control of magma volatile content and chamber depth on the mass erupted during explosive volcanic eruptions. *Journal of Geophysical Research*, **102**, 10 273–10 290.

Buiter, S. J. H., Yu, A. *et al.* 2006. *The Numerical Sandbox: Comparison of Model Results for a Shortening and an Extension Experiment, Analogue and Numerical Modelling of Crustal-Scale Processes*. Geological Society, London, Special Publications, **253**, 29–64.

Burov, E. & Guillou-Frottier, L. 1999. Thermomechanical behavior of large ash flow calderas. *Journal of Geophysical Research*, **104**, 23 081–23 109.

Burov, E., Jaupart, C. & Guillou-Frottier, L. 2003. Ascent and emplacement of buoyant magma bodies in brittle–ductile upper crutst. *Journal of Geophysical Research*, **108**, 2177.

Caquot, A. & Kerisel, J. 1956. *Traité de Mécanique des Sols*. Gauthier-Villars, Paris.

Chery, J., Bonneville, A., Villote, J. P. & Yuen, D. 1991. Numerical modeling of caldera dynamical behaviour. *Geophysical Journal International*, **105**, 365–379.

Chery, J., Zoback, M. D. & Hassani, R. 2001. An integrated mechanical model of the San Andreas Fault in central and northern California. *Journal of Geophysical Research*, **106**, 22 051–22 066.

Cundall, P. A. 1989. Numerical experiments on localization in frictional materials. *Ingenior Archives*, **59**, 148–159.

Cundall, P. & Board, M. 1988. A microcomputer program for modeling large-strain plasticity problems. *Numerical Methods in Geomechanics*, **6**, 2101–2108.

Day, S. J. 1996. Hydrothermal pore fluid pressure and the stability of porous, permeable volcanoes. *In*: McGuire, W. J., Jones, A. P. & Neuber, J. (eds) *Volcano Stability on the Earth and Other Planets*. Geolocal Society, London, Special Publications, **110**, 77–93.

D'Escatha, Y. & Mandel, J. 1974. Stabilité d'une galerie peu profonde en terrain meuble. *Industrie Minerale*, Numero Special, 45–53.

Ellis, S. M., Wilson, C. J. N., Bannister, S., Bibby, H. M., Heise, W., Wallace, L. & Patterson, N. 2007. A future magma inflation event under the rhyolitic Taupo volcano, New Zealand: numerical models based on constraints from geochemical, geological and geophysical data. *Journal of Volcanology and Geothermal Research*, **168**, 1–27.

Engelder, T. & Leftwich, J. T. 1997. A pore-pressure limit in overpressured South Texas oil and gas field. *In*: Surdam, R. C. (ed.) *Seals, Traps, and the Petroleum System*. American Association of Petroleum Geologists, Tulsa, Memoir 67, Chapter 15, 255–267.

Fairhurst, C. & Carranza-Torres, C. 2002. Closing the circle, some comments on design procedures for tunnel supports in rock. *In*: Labuz, J. F. & Bentler, J. G. (eds) *Proceedings, University of Minnesota 50th Annual Geotechnical Conference,* Minneapolis University, Minnesota, 21–84.

Fialko, Y., Khazan, Y. & Simons, M. 2001. Deformation due to a pressurized horizontal circular crack in an elastic half-space, with applications to volcano geodesy. *Geophysical Journal International*, **146**, 181–190.

Foroozan, R., Elsworth, D., Voight, B. & Mattioli, G. S. 2010. Dual reservoir structure at Soufrière Hills volcano inferred from continuous GPS observations and heterogeneous elastic modeling. *Geophysical Research Letters*, **37**, doi: 10.1029/2010GL042511.

Galgana, G. A., McGovern, P. J. & Grosfils, E. B. 2011. Evolution of large Venusian volcanoes: insights from coupled models of lithospheric flexure and magma reservoir pressurization. *Journal of Geophysical Research*, **116**, E03009, doi: 10.1029/2010JE 003654.

Gerbault, M., Poliakov, A. & Daignières, M. 1998. Prediction of faulting from the theories of elasticity and plasticity: what are the limits? *Journal of Structural Geology*, **20**, 301–320.

Gerbault, M., Cappa, F. & Hassani, R. 2012. Elastoplastic and hydromechanical models of failure around an infinitely long magma chamber. *Geochemistry Geophysics Geosystems*, **13**, Q03009, doi: 10.1029/2011GC003917.

Geyer, A. & Marti, J. 2009. Stress fields controlling the formation of nested and overlapping calderas: implications for the understanding of caldera unrest. *Journal of Volcanology and Geothermal Research*, **181**, 185–195.

Gray, J. P. & Monaghan, J. J. 2004. Numerical modeling of stress fields and fracture around magma chambers. *Journal of Volcanology and Geothermal Research*, **135**, 259–283.

Gressier, J.-B., Mourgues, R., Bodet, L., Matthieu, J.-Y., Galland, O. & Cobbold, P. 2010. Control of pore fluid pressure on depth of emplacement of magmatic sills: an experimental approach. *Tectonophysics*, **489**, 1–12.

Grosfils, E. B. 2007. Magma reservoir failure on the terrestrial planets: assessing the importance of gravitational loading in simple elastic models. *Journal of Volcanology and Geothermal Research*, **166**, 47–75.

GUDMUNDSSON, A. 1988. Effect of tensile stress concentration around magma chambers on intrusion and extrusion frequencies. *Journal of Volcanology and Geothermal Research*, **35**, 179–194.

GUDMUNDSSON, A. 2006. How local stresses control magma-chamber ruptures, dyke injections, and eruptions in composite volcanoes. *Earth-Science Reviews*, **79**, 1–31.

GUDMUNDSSON, A., MARIF, J. & TURON, E. 1997. Stress field generating ring faults in volcanoes. *Geophysical Research Letters*, **24**, 1559–1562.

GUDMUNDSSON, A., FJELDSKAAR, I. & BRENNER, S. L. 2002. Propagation pathways and fluid transport of hydrofractures in jointed and layered rocks in geothermal fields. *Journal of Volcanology and Geothermal Research*, **116**, 257–278.

GUILLOU-FROTTIER, L., BUROV, E. B. & MILESI, J. P. 2000. Genetic links between ash flow calderas and associated ore deposits as revealed by large-scale thermo-mechanical modeling. *Journal of Volcanology and Geothermal Research*, **102**, 339–361.

HAFNER, W. 1951. Stress distribution and faulting. *Bulletin of the Geological Society of America*, **62**, 373–398.

HARDY, S. 2008. Structural evolution of calderas: insights from two-dimensional discrete element formulations? *Geology*, **36**, 927–930.

HASSANI, R., JONGMANS, D. & CHÉRY, J. 1997. Study of plate deformation and stress in subduction processes using two-dimensional numerical models. *Journal of Geophysical Research* **102**, 17 951–17 965.

HENRY, C. D., KUNK, M. J., MUEHLBERGER, W. R. & MCINTOSH, W. C. 1997. Igneous evolution of a complex laccolith-caldera, the Solitario, Trans-Pecos Texas: implications for calderas and subjacent plutons. *Geological Society of America Bulletin*, **10**, 1036–1054.

HILLIS, R. R. (ed.) 2003. *Pore Pressure/Stress Coupling and its Implications for Rock Failure*. Geological Society, London, Special Publications, **216**, 359–368, doi: 10.1144/GSL.SP.2003.216.01.23

HOLOHAN, P., TROLL, V. R., ERRINGTON, M., DONALDSON, C. H., NICOLL, G. R. & EMELEUS, C. H. 2009. The Southern Mountains Zone, Isle of Rum, Scotland: volcano-sedimentary processes upon an uplifted and subsided magma chamber roof. *Geological Magazine*, **146**, 400–418.

HUBBERT, M. K. & RUBEY, W. W. 1959. Role of fluid pressure in mechanics of overthrust faulting. *Geological Society of America Bulletin*, **70**, 115–166.

HUPPERT, H. & WOODS, A. W. 2002. The role of volatiles in magma chamber dynamics. *Nature*, **420**, 493–495.

HURWITZ, D. H., LONG, S. M. & GROSFILS, E. B. 2009. The characteristics of magma reservoir failure beneath a volcanic edifice. *Journal of Volcanology and Geothermal Research*, **188**, 379–394, doi: 10.1016/j.jvolgeores.2009.10.004.

JEFFERY, J. B. 1920. Plane stress and plane strain in bi-polar coordinates. *Transactions of the Royal Society, London*, **221**, 265–293.

KARLSTROM, L., DUFEK, J. & MANGA, M. 2010. Magma chamber stability in arc and continental crust. *Journal of Volcanology and Geothermal Research*, **190**, 249–270; doi: 10.1016/j.jvolgeores.2009.10.003.

KAUS, B. 2010. Factors that control the angle of shear bands in geodynamic numerical models of brittle deformation. *Tectonophysics*, **484**, 36–47.

KUMAGAI, H., PLACIOS, P., RUIZ, M., YEPES, H. & KOZONO, T. 2011. Ascending seismic source during an explosive eruption at Tunguruhua volcano, Ecuador. *Geophysical Research Letters*, **38**, L01306, doi: 10.1029/2010GL045944.

KUSUMOTO, S. & TAKEMURA, K. 2003. Numerical simulation of caldera formation due to collapse of a magma chamber. *Geophysical Research Letters*, **30**, doi: 10.1029/2003GL018380.

LAFRANCE, B. & JOHN, B. E. 2001. Sheeting and dyking emplacement of the Gunnison annular complex, SW Colorado. *Journal of Structural Geology*, **23**, 1141–1150.

LAVIER, L., BUCK, W. & POLIAKOV, A. 2000. Factors controlling normal fault offset in an ideal brittle layer. *Journal of Geophysical Research*, **105**, 23 431–23 442.

LISTER, J. R. & KERR, R. C. 1991. Fluid-mechanical models of crack propagation and their application to magma transport in dykes. *Journal of Geophysical Research*, **96**, 10 049–10 077.

MARTI, J., GEYER, A., FOLCH, A. & GOTTSMANN, J. 2008. A review of collapse caldera modeling. *In*: *Developments in Volcanology*, **10**, doi: 10.1016/S1871-644X(07)00006-X, 233–283.

MASEK, J. G. & DUNCAN, C. C. 1998. Minimum-work mountain building. *Journal of Geophysical Research*, **103**, 907–917.

MASSINAS, S. A. & SAKELLARIOU, M. G. 2009. Closed-form solution for a plastic zone formation around a circular tunnel in half-space obeying Mohr–Coulomb criterion. *Géotechnique*, **59**, 691–701, doi: 101680/geot8.069.

MASTERLARK, T. 2007. Magma intrusion and deformation predictions: sensitivities to the Mogi assumptions. *Journal of Geophysical Research*, **112**, doi: 10.1029/2006JB004860.

MASTERLARK, T. & LU, Z. 2004. Transient volcano deformation sources imaged with interferometric synthetic aperture radar: application to Seguam Island, Alaska. *Journal of Geophysical Research*, **109**, doi: 10.1029/2003JB002568.

MAZA, M., BRIQUEU, L., DAUTRIA, J.-M. & BOSCH, D. 1998. Le complexe annulaire d'age Oligocene de l'Achkal (Hogggar Central, Sud Algerie): temoin de la transition au Cenozoique entre les magmastismes tholeitique et alcalin. Evidences par les isotopes du Sr, Nd, Pb. *Comptes Rendus de l'Académie des Sciences – Series IIA*, **327**, 167–172, doi: 10.1016/S1251-8050(98)80004-9.

MCLEOD, P. & TAIT, S. 1999. The growth of dyke from magma chambers. *Journal of volcanology and Geothermal Research*, **92**, 231–245.

MOGI, K. 1958. Relations between the eruption of various volcanoes and the deformation of the ground surfaces around them. *Bulletin of the Earthquake Research Institute*, **36**, 99–134.

NADAI, A. 1950. *The Theory of Flow and Fracture of Solids*. McGraw-Hill, New York.

PARFITT, E. A., WILSON, L. & HEAD, J. W. 1993. Basaltic magma reservoirs: Factors controlling their rupture characteristics and evolution. *Journal of Volcanology and Geothermal Research*, **55**, 1–14, doi: 10.1016/0377-0273(93)90086-7.

PINEL, V. & JAUPART, C. 2003. Magma chamber behavior beneath a volcanic edifice. *Journal of Geophysical Research*, **108**, doi: 10.1029/2002JB001751.

PINEL, V. & JAUPART, C. 2005. Caldera formation by magma withdrawal from a reservoir beneath a volcanic edifice. *Earth and Planetary Science Letters*, **230**, 273–287.

PODLADCHIKOV, Y., POLIAKOV, A. & CUNDALL, P. 1993. An explicit inertial method for the simulation of visco-elastic flow: an evaluation of elastic effects on diapiric flow. *Flow and Creep in the Solar System: Observation, Modeling and Theory*, **391**, 175–195.

POLIAKOV, A. & PODLADCHIKOV, Y. 1992. Diapirism and topography. *Geophysical Journal International*, **109**, 553–564.

PRITCHARD, M. E. & SIMONS, M. 2004. An insar-based survey of volcanic deformation in central Andes. *Geochemistry Geophysics Geosystems*, **5**, doi: 10.1029/2003GC000610.

RAMSEY, J. M. & CHESTER, F. M. 2004. Hybrid fracture and the transition from extension fracture to shear fracture. *Nature*, **428**, 63–66.

REGENAUER-LIEB, K. & PETIT, J. P. 1997. Cutting of the European continental lithosphere: plasticity theory applied to the Alpine collision. *Journal of Geophysical Research*, **102**, 7731–7746.

RIVALTA, E. & SEGALL, P. 2008. Magma compressibility and the missing source for some dike intrusions. *Geophysical Research Letters*, **35**, L04306, doi: 10.1029/2007GL032521.

ROCHE, O. & DRUITT, T. H. 2001. Onset of caldera collapse during ignimbrite eruptions. *Earth and Planetary Science Letters*, **191**, 191–202.

RUBIN, A. M. 1995. Propagation of magma-filled cracks. *Annual Review, Earth and Planetary Sciences*, **23**, 287–336.

RUBIN, A. M. & POLLARD, D. D. 1987. Origins of blade-like dikes in volcanic rift zones. *US Geological Survey Professional Paper*, **1350**, 1449–1470.

DE SAINT BLANQUAT, M., HORSMAN, E., HABERT, G., MORGAN, S., VANDERHAEGHE, O., LAW, R. & TIKOFF, B. 2011. Multiscale magmatic cyclicity, duration of pluton construction, and the paradoxical relationship between tectonism and plutonism in continental arcs. *Tectonophysics*, **500**, 20–33.

SALENÇON, J. 1966. Expansion quasi-statique d'une cavité à symétrie sphérique ou cylindrique dans un milieu élastoplastique. *Annales des Ponts et Chaussées*, **III**, 175–187.

SALENÇON, J. 1969. *La théorie des charges limites dans la résolution des problèmes de plasticité en déformation plane*. PhD thesis, Laboratoire de Mécanique des Solides de l'École Polytechnique, Paris.

SARTORIS, G., POZZI, J. P., PHILIPPE, C. & LE MOUEL, J. L. 1990. Mechanical instability of shallow magma chambers. *Journal of Geophysical Research*, **95**, 5141–5151.

SEGALL, P. 2009. *Earthquake and Volcano Deformation*. Princeton University Press, Princeton.

STURKELL, E., SIGMUNDSSON, F. & SLUNGA, R. 2006. 1983–2003 decaying rate of deflation at Askja caldera: pressure decrease in an extensive magma plumbing system at a spreading plate boundary. *Bulletin of Volcanology*, **68**, 727–735, doi: 10.1007/s00445-005-0046-1.

TAIT, S., JAUPART, C. & VERGNIOLLE, S. 1989. Pressure, gas content and eruption periodicity of a shallow, crystallizing magma chamber. *Earth and Planetary Science Letters*, **92**, 107–123.

TAPPONNIER, P. & MOLNAR, P. 1976. Slip-line field theory and large-scale continental tectonics. *Nature*, **264**, 319–324.

TIMOSHENKO, S. & GOODIER, J. N. 1970. *Theory of Elasticity*. 2nd edn. McGraw-Hill Higher Education, New York.

TOWNEND, J. & ZOBACK, M. D. 2000. How faulting keeps the crust strong. *Geology*, **28**, 399–402.

TRASATTI, E., GIUNCHI, C. & BONAFEDE, M. 2005. Structural and rheological constraints on source depth and overpressure estimates at the Campi flegrei caldera, Italy. *Journal of Volcanology and Geothermal Research*, **144**, 105–118.

TURCOTTE, D. & SCHUBERT, G. 1982. *Geodynamics: Applications of Continuum Physics to Geological Problems.* Wiley, New York.

VERMEER, P. A. & DE BORST, R. 1984. Non-associated plasticity for soils, concrete and rocks. *Heron,* **29**, 1–75.

VERRUIJT, A. 1998. Deformations of an elastic half plane with a circular cavity. *International Journal of Solids Structures*, **35**, 2795–2804.

WAITE, G. P. & SMITH, R. B. 2002. Seismic evidence for fluid migration accompanying susbsidence of the Yellowstone caldera. *Journal of Geophysical Research*, **107**, doi: 10.1029/2001JB000586.

WEGLER, U., LÜHR, B.-G., SNIEDER, R. & RATDOMOPURBO, A. 2006. Increase of shear wave velocity before the 1998 eruption of Merapi volcano (Indonesia). *Geophysical Research Letters*, **333**, doi: 10.1029/2006GL025928,2006.

WHITE, B. G., LARSON, M. K. & IVERSON, S. R. 2004. Origin of mining-induced fractures through macro-scale distortion. *In*: *Gulf Rocks 2004. Rock Mechanics across Borders and Disciplines.* Proceedings of the Sixth North American Rock Mechanics Conference. Houston, Texas. Report ARMA/NARMS 04-569.

WOODCOCK, N. H. & UNDERHILL, J. R. 1987. Emplacement-related fault patterns around the Northern granite, Arran, Scotland. *Geological Society of America Bulletin*, **98**, 515–527.

YARUSHINA, V. M., DABROWSKI, M. & PODLADCHIKOV, Y. Y. 2010. An analytical benchmark with combined pressure and shear loading for elastoplastic numerical models. *Geochemistry Geophysics Geosystems*, **11**, doi: 10.1029/2010GC003130.